JACS
JOURNAL OF THE AMERICAN CHEMICAL SOCIETY
pubs.acs.org/JACS
Article

Dynamic Nuclear Polarization Enables NMR of Surface Passivating Agents on Hybrid Perovskite Thin Films

Aditya Mishra, Michael A. Hope,* Masaud Almalki, Lukas Pfeifer, Shaik Mohammed Zakeeruddin, Michael Grätzel, and Lyndon Emsley*

Cite This: J. Am. Chem. Soc. 2022, 144, 15175−15184
Read Online
ACCESS | Metrics & More | Article Recommendations | Supporting Information

ABSTRACT: Surface and bulk molecular modulators are the key to improving the efficiency and stability of hybrid perovskite solar cells. However, due to their low concentration, heterogeneous environments, and low sample mass, it remains challenging to characterize their structure and dynamics at the atomic level, as required to establish structure−activity relationships. Nuclear magnetic resonance (NMR) spectroscopy has revealed a wealth of information on the atomic-level structure of hybrid perovskites, but the inherent insensitivity of NMR severely limits its utility to characterize thin-film samples. Dynamic nuclear polarization (DNP) can enhance NMR sensitivity by orders of magnitude, but DNP methods for perovskite materials have so far been limited. Here, we determined the factors that limit the efficiency of DNP NMR for perovskite samples by systematically studying layered hybrid perovskite analogues. We find that the fast-relaxing dynamic cation is the major impediment to higher DNP efficiency, while microwave absorption and particle morphology play a secondary role. We then show that the former can be mitigated by deuteration, enabling ^{1}H DNP enhancement factors of up to 100, which can be harnessed to enhance signals from dopants or additives present in very low concentrations. Specifically, using this new DNP methodology at a high magnetic field and with small sample volumes, we have recorded the NMR spectrum of the 20 nm (6 μg) passivating layer on a single perovskite thin film, revealing a two-dimensional (2D) layered perovskite structure at the surface that resembles the n = 1 homologue but which has greater disorder than in bulk layered perovskites.

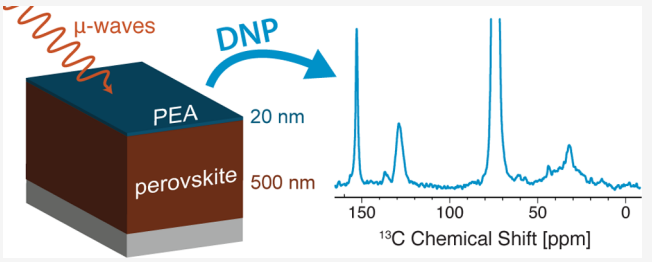

INTRODUCTION

Hybrid organic−inorganic perovskites have emerged as a promising alternative to existing solar cell technologies owing to their bandgap tunability,[1−3] facile processing methods,[4,5] and competitive performance.[6−11] The perovskite crystal structure consists of an A-site cation (e.g., formamidinium, FA^+, $CH(NH_2)_2^+$; methylammonium, MA^+, $CH_3NH_3^+$) in a three-dimensional (3D) network of lead halide octahedra as shown in Figure 1a. As the photoactive phases of hybrid perovskite materials are not intrinsically stable under ambient conditions,[12] methods to stabilize them are of intense current interest, with strategies based today either on elemental doping with inorganic cations (Cs^+, K^+, Rb^+, Mn^{2+}, Co^{2+}, Sb^{3+}, In^{3+})[13−15] or on passivation by a surface treatment of organic molecules or salts.[14−19] When bulky molecular cations are used, two-dimensional (2D) layered perovskites can form where inorganic perovskite slabs are separated by layers of organic cations (Figure 1a).[20−24] Bulk layered perovskites are more stable than their 3D counterparts but typically have lower photoconversion efficiencies.[24,25] 2D/3D heterostructures, where the layered perovskite forms at the surface of the bulk perovskite, combine the higher stability provided by the 2D phase and the superior optoelectronic properties of the 3D perovskite, while further passivating interfacial vacancies to reduce nonradiative recombination.[26−29] The detailed manner in which organic moieties interact with the perovskite structure has been thought to modify the energy landscape of the material and thereby template the photoactive α-$FAPbI_3$ phase.[6,30,31]

Establishing structure−activity relationships to optimize perovskite stability requires a detailed knowledge of the atomic-level local structure for these dopants and surface treatments when applied to perovskite materials. Although diffraction-based techniques can be used to study the inorganic lattice, due to the polycrystalline nature of solution-processed thin films and the lack of long-range order for surface and/or bulk dopants and additives, it is difficult to determine structural information for these minor species using diffraction-based methods.

Received: May 19, 2022
Published: August 12, 2022

ACS Publications
© 2022 The Authors. Published by American Chemical Society

https://doi.org/10.1021/jacs.2c05316
J. Am. Chem. Soc. 2022, 144, 15175−15184

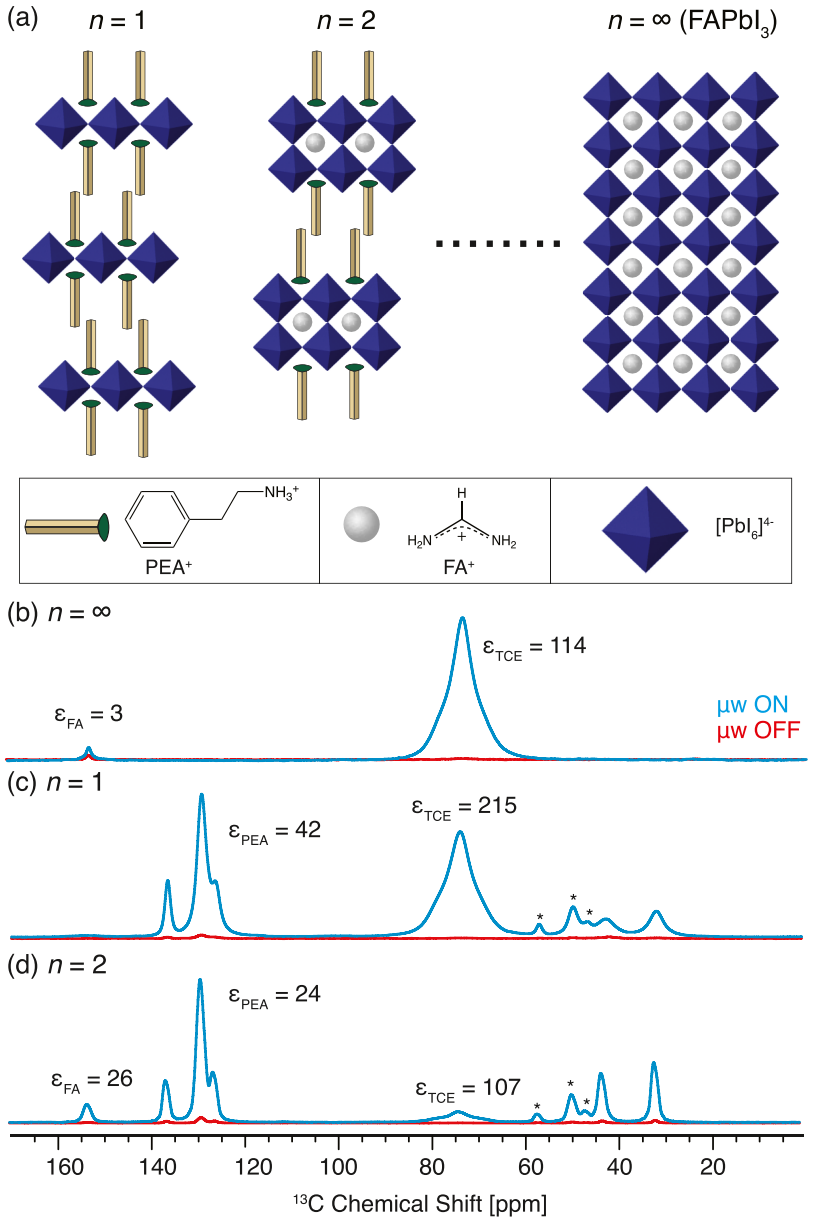

Figure 1. (a) Schematic representation of the layered Ruddlesden−Popper perovskite structures. (b−d) DNP-enhanced $^{1}H \rightarrow {}^{13}C$ CP spectra with and without microwave (μw) irradiation of (b) $FAPbI_3$ ($n = \infty$) at 133 K, (c) PEA_2PbI_4 ($n = 1$) at 119 K, and (d) $PEA_2FAPb_2I_7$ ($n = 2$) at 130 K. All temperatures are given within ±2 K. Asterisks indicate spinning sidebands. The μw on spectra shown in the figure were recorded with 8 ($n = \infty$), 64 ($n = 1$), and 4 ($n = 2$) scans each and a polarization delay of 100 s between scans. The full details are given in the Experimental Section.

Nuclear magnetic resonance (NMR) is well suited to establish an atomic-level understanding of both the organic and inorganic components of hybrid perovskites, as well as dopants and additives.[32−35] Specifically, magic angle spinning (MAS) NMR has previously been applied to study cation incorporation,[36−41] phase segregation,[38,42−47] cation dynamics,[48−51] passivating layers,[31,52] degradation,[52,53] and phase transitions.[48−51] NMR has also been successful in probing bulk layered perovskites,[47,54,55] bulk 2D/3D perovskite heterostructures,[56−59] and the surfaces of perovskite nanocrystals.[60−62] However, the intrinsic insensitivity of NMR limits its utility to study thin-film samples as used in perovskite devices, owing to the very low sample mass. This insensitivity is compounded for the study of dopants and additives, which comprise only a small fraction of the sample. Consequently, in the majority of previous studies, either several thick films or mechanosynthesized powders were used to enable NMR experiments to be performed. Thus, key challenges relating to NMR sensitivity in hybrid perovskites remain,[32] with spectra from the surface and interface species in thin films still largely out of reach.

To overcome the intrinsic sensitivity problem associated with NMR and solve structural problems in materials science, dynamic nuclear polarization (DNP) methods have been developed.[63−67] In these experiments, the target material is wetted with a solution of stable biradicals and cooled to ∼100 K.[65] Continuous microwave irradiation at or near the electron spin resonance (ESR) frequency transfers the high electron polarization from the radical to solvent nuclei, which can then be transferred to surface species on the target material or propagate into the bulk by spin diffusion, enhancing the corresponding NMR signal in both cases.[65] This DNP

https://doi.org/10.1021/jacs.2c05316
J. Am. Chem. Soc. 2022, 144, 15175−15184

approach has been successfully applied to study surfaces and interfaces in materials for batteries,[68,69] catalysis,[70−75] and optoelectronics.[76]

Sensitivity-enhancing protocols for hybrid perovskites have been investigated by Hanrahan et al.[77] For the detection of ^{207}Pb spectra, they found the most promising technique to be proton detection, while MAS DNP was surprisingly inefficient for both the organic and inorganic components: signal enhancements were typically <10, especially in the case of the most technologically relevant iodide perovskite.[77] A clear understanding of the underlying challenges in applying DNP to organic−inorganic perovskites, and methodologies to overcome them, are still lacking.

Here, we demonstrate efficient DNP for the organic moieties in layered hybrid organic−inorganic perovskites. Specifically, we systematically investigate a class of 2D perovskite homologues to determine that the dynamic A-site cations are the main cause of poor DNP performance. We then demonstrate how to overcome this with deuteration strategies, enabling ^{1}H DNP enhancement factors of up to a factor 100. Finally, using the DNP methodology developed for the layered perovskite combined with a high magnetic field and small sample volumes, we have successfully recorded the NMR spectrum of the surface coating (∼20 nm) deposited on a single $FAPbI_3$ perovskite thin-film sample (2 × 2 cm^2 area). This opens the door to detailed atomic-level structural studies of surface treatments on technologically relevant samples.

RESULTS AND DISCUSSION

First, we determined the DNP enhancements that can be achieved for the organic FA^+ cation in bulk $FAPbI_3$ using a conventional DNP formulation, i.e., impregnation of the materials with 16 mM TEKPol[78] in tetrachloroethane (TCE) at ∼100 K[64,79] (note that $FAPbI_3$ undergoes phase transitions at ∼140 and ∼285 K).[49,80] As shown in Figure 1b, although the enhancement factor upon microwave irradiation for the ^{1}H of the TCE is 114 (as measured through the ^{13}C signal intensity in a ^{1}H→^{13}C cross-polarization (CP) spectrum), the FA^+ cation signal exhibits an enhancement of only ∼3. While this does correspond to an experimental time saving by an order of magnitude, for typical surfaces or even for bulk microcrystalline solids, ^{1}H DNP enhancement factors >30 can routinely be achieved today.[81−83] Furthermore, the solvent enhancement is also lower than the expected factor of ∼200 for this formulation. Overall, DNP experiments do not work as well as expected in this hybrid perovskite.

There are several factors that could explain the poor DNP performance in α-$FAPbI_3$. It is well established that the organic cation that occupies the cuboctahedral cavity in organic−inorganic perovskites is highly dynamic.[48−50] At 100 K, this motion occurs on a similar timescale to the ^{1}H Larmor frequency (∼1 ns), resulting in fast ^{1}H relaxation ($T_1 \approx 1$ s). As a result, the cations can act as polarization sinks, causing the hyperpolarization to relax before it can diffuse significantly into the particles. Alternatively, the perovskite material could absorb the microwave radiation itself due to the contribution of the dynamic cation to the dielectric properties.[84] This can have two main consequences: (i) an overall reduction in the available microwave energy to drive the ESR transitions and/or (ii) a significant increase in the sample temperature, resulting in shorter electron spin relaxation times and less-efficient DNP (note that while the increased temperature does affect the cation dynamics, there is little change in the ^{1}H T_1 due to the proximity to the T_1 minimum; Figure S6). Each of these factors could play a significant role in determining the overall enhancement in the perovskite materials, and in the following, we disentangle their relative contributions.

To distinguish between these factors, we performed experiments on samples of two-dimensional Ruddlesden−Popper layered perovskites containing phenylethylammonium (PEA^+) spacers,[85,86] which allow the dynamic FA^+ cation to be removed and systematically reintroduced in the different homologues. These low-dimensional perovskites are characterized by the number of inorganic layers per organic layer (n), as shown in Figure 1a. In this convention, α-$FAPbI_3$ can be considered as $n = \infty$. Notably, the $n = 1$ member is unique in that it does not contain an A-site cation and therefore offers the advantage to selectively investigate the effects of the mobile FA^+ cation.

Figure 1c shows the DNP enhanced ^{1}H→^{13}C CP spectrum of $n = 1$ (PEA_2PbI_4) where we observe enhancement factors of 215 and 43 for the solvent and PEA^+ signals, respectively (see Figure S1 for the spectral assignment). This is around the maximum solvent enhancement that can be achieved for this formulation, and the perovskite enhancement is far higher than for pure α-$FAPbI_3$ (see the summary in Figure 2a). The lower

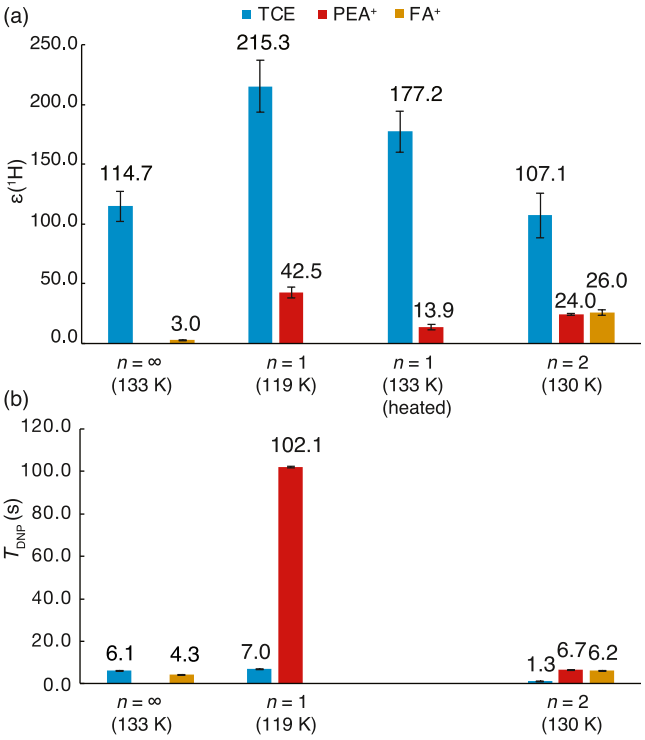

Figure 2. Comparison of (a) ^{1}H DNP enhancement factors and (b) T_{DNP} values measured via ^{1}H→^{13}C CP spectra of $n = \infty$ ($FAPbI_3$), $n = 1$ (PEA_2PbI_4), and $n = 2$ ($PEA_2FAPb_2I_7$) at the specified temperatures. Temperatures are given within ±2 K.

enhancement of PEA^+ compared to the solvent is expected since the high polarization from the wetting phase has to diffuse into the particle.[63,87,88] For the $n = 2$ ($PEA_2FAPb_2I_7$) composition (Figure 1d), the solvent enhancement is significantly lower (107), whereas the perovskite enhancements are still appreciable (around 25). Notably, the FA^+ and PEA^+ moieties show very similar enhancement factors within error since they are in atomic-scale proximity and fast ^{1}H−^{1}H

https://doi.org/10.1021/jacs.2c05316
J. Am. Chem. Soc. 2022, 144, 15175−15184

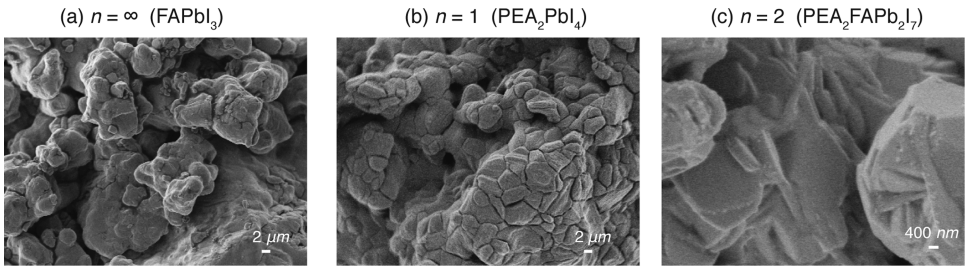

Figure 3. SEM images of mechanosynthesized (a) $n = \infty$ ($FAPbI_3$), (b) $n = 1$ (PEA_2PbI_4), and (c) $n = 2$ ($PEA_2FAPb_2I_7$) perovskites.

spin diffusion equalizes the nuclear hyperpolarization.[87,88] These large DNP enhancements for both the $n = 1$ and $n = 2$ perovskites further allow $^1H \rightarrow ^{15}N$ CP spectra to be measured within minutes (Figure S2).

The observation that the solvent enhancements for the $n = 2$ and $n = \infty$ samples are similar, while that for $n = 1$ is higher, is consistent with the presence of dynamic FA^+ cations in the former; we now examine the mechanism for this. First, we consider microwave heating: for $n = 2$ and $n = \infty$, the microwaves induce heating by 30 ± 2 and 33 ± 2 K, respectively, resulting in a minimum achievable temperature of 133 ± 2 K, whereas for $n = 1$ the heating is only 19 ± 2 K, resulting in a minimum achievable temperature of 119 ± 2 K. Clearly, the presence of the dynamic FA^+ cation does induce greater sample heating. However, when the sample temperature is deliberately increased to 130 ± 2 K for the $n = 1$ sample by heating the incident gas flows, the solvent enhancement decreases only to 177, still far higher than for the $n = 2$ and $n = \infty$ perovskites. Therefore, while sample heating does play a role, it is not the major cause of the differing DNP performance.

Further details on the DNP behavior can be inferred from the buildup of nuclear polarization under microwave irradiation, as characterized by the time constant T_{DNP} (Figure 2b). The long T_{DNP} for the $n = 1$ sample is consistent with the high enhancement, since there is more time to accumulate polarization, which relaxes more slowly. T_{DNP} is significantly shorter for the $n = 2$ and $n = \infty$ perovskites, consistent with the presence of fast-relaxing FA^+ cations. However, despite the similar build-up behavior, the enhancement is far higher for $n = 2$ than for $n = \infty$. This difference can be explained by considering another crucial factor for DNP of impregnated solids, the particle size and morphology;[87,88] therefore, scanning electron microscopy (SEM) images were obtained as shown in Figure 3.

The $n = \infty$ and $n = 1$ compositions show loosely agglomerated secondary particles composed of approximately spherical primary particles with an average particle size of 0.7 ± 0.2 μm (Figure 3a,b). In contrast, the $n = 2$ sample (Figure 3c) exhibits platelet-like primary particles, as commonly observed for layered materials,[59] with a thickness of 0.13 ± 0.05 μm. The morphology in the $n = 2$ sample favors the propagation of polarization to the bulk owing to the increased surface-to-volume ratio and the shorter diffusion lengths required.[87,88] Therefore, although the FA^+ cation reduces the T_1 and therefore the spin-diffusion length for the $n = 2$ homologue, the favorable thin particle size nevertheless allows appreciable hyperpolarization to be relayed to the perovskite.

To determine, and mitigate, the effect of fast ^1H relaxation by the dynamic FA^+ cation, we synthesized the $n = 2$ perovskite having deuterated the FA^+ cation to different degrees. Note that since the $-NH_3$ hydrogens in PEA^+ could exchange with FA^+ during synthesis, these were also deuterated. Deuteration of the DNP matrix to decrease the ^1H heat capacity is well established,[88−90] while deuteration of fast-relaxing methyl groups in proteins[91] or on the surfaces of heterogeneous catalysts[92] has also previously been shown to improve DNP performance. Figure 4a shows how with increasing deuteration of FA^+, the enhancement of the solvent increases progressively, to reach levels similar to the factors of 177−215 achieved for $n = 1$. This indicates that dissipation of hyperpolarization in the fast-relaxing perovskite phase is the primary factor limiting the solvent enhancement in the $n = 2$ formulations. The concomitant increase in the T_{DNP} constants for the perovskite corroborates this observation (Figure 4b), since the ratio of fast-relaxing FA^+ protons to slower relaxing PEA^+ protons decreases. For the sample with medium deuteration, the enhancement of the perovskite signals increases by a factor of 4 to over 100 for the PEA^+, as compared to the nondeuterated sample. This arises from the lower proportion of the fast-relaxing cations, which slows the average T_1 relaxation, increasing the spin-diffusion length and the amount of hyperpolarization that can accumulate both in the solvent and the perovskites. Interestingly, the highly deuterated sample exhibits even higher solvent enhancements, but lower enhancements for the perovskite, comparable to the nondeuterated $n = 2$ sample. This can be explained by a reduction in ^1H spin-diffusion efficiency at the highest deuteration level due to the low ^1H concentration, which hampers the propagation of polarization into the perovskite. In particular, when the FA^+ cation is highly deuterated, the perovskite layer acts as a barrier to ^1H spin diffusion. Furthermore, since the layers are likely to be aligned with the platelet morphology, we speculate that polarization from the majority of the hyperpolarized solvent must pass through FA^+ layers. Therefore, although the high deuteration of FA^+ moieties increases the perovskite T_{DNP} and reduces polarization loss by relaxation, the overall effect with diminished spin diffusion gives similar enhancements to those of the nondeuterated $n = 2$ composition.

Applying a similar deuteration strategy to pure $FAPbI_3$ is less successful. The solvent enhancement is increased to some extent but not as much as for $n = 2$ (Figure 4c); this is ascribed to the fact that the T_1 relaxation of the perovskite remains fast (T_{DNP} = 4 s, Figure 4d), and therefore, although the concentration of the relaxation sinks is reduced, the perovskite does still act as a sink for the solvent hyperpolarization. Greater microwave absorption by $n = \infty$ than by $n = 2$ reducing the efficiency of saturating the ESR transitions could also play a role, although the sample heating remains similar. The low enhancement for the perovskite itself is expected because only

https://doi.org/10.1021/jacs.2c05316
J. Am. Chem. Soc. 2022, 144, 15175−15184

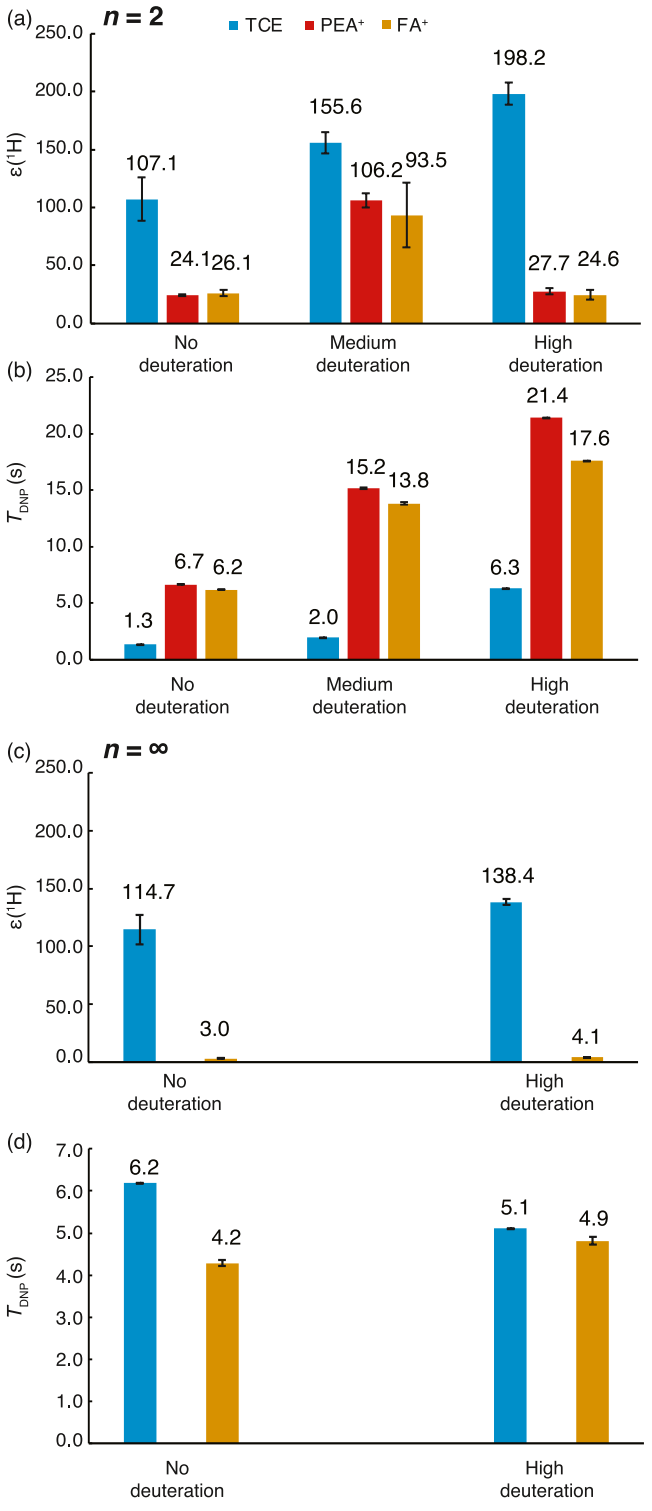

Figure 4. ^{1}H DNP enhancement factors and polarization build-up constants (T_{DNP}) as a function of deuteration level for (a, b) n = 2 $PEA_2FAPb_2I_7$ and (c, d) n = ∞ $FAPbI_3$. Medium deuteration for n = 2 is achieved using 60% d_3-PEAI and 50% d_4-FAI. High deuteration for n = 2 is achieved using 80% d_3-PEAI and 85% d_5-FAI. High deuteration for $FAPbI_3$ is achieved using 85% d_5-FAI.

the fast-relaxing cations with residual protonation can be observed.

Although these DNP experiments significantly improve the NMR sensitivity, they were performed with conventional DNP hardware using 3.2 mm outer diameter sample containers (rotors) that require a high sample mass of at least 50 mg, whereas a typical thin-film device contains only ∼1 mg of perovskite. Very recently, state-of-the-art DNP hardware has been developed using 0.7 mm outer diameter rotors that require only 1−2 mg of sample, while enabling faster magic-angle spinning that improves resolution;[93] sensitivity and resolution are further improved by the use of a high magnetic field of 21 T, compared to 9.4 T used above. We first tested the DNP using this system on a mechanosynthesized n = 1 perovskite sample, as studied above, wetted with a 32 mM solution of the HyTEK-2 biradical[94] in TCE, which has been shown to perform significantly better than TEKPol at a high field with fast spinning.[93] As shown in Figure 5a, the TCE and

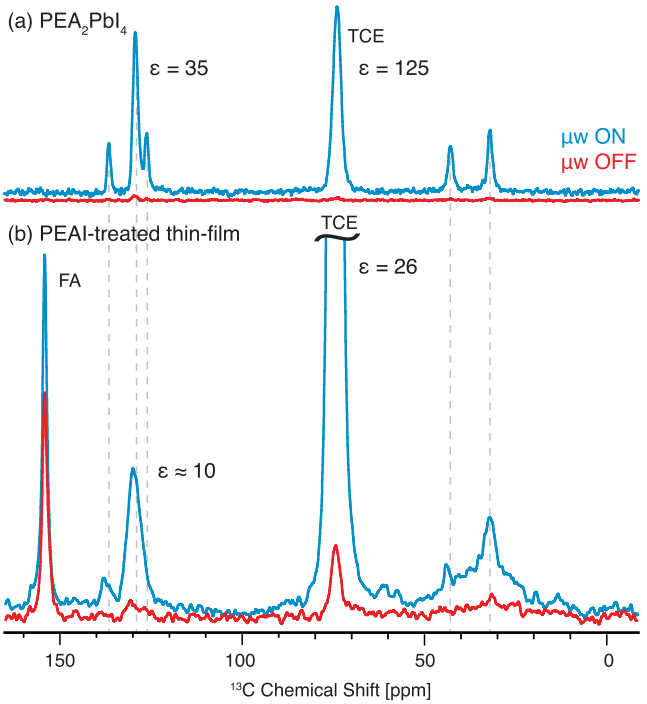

Figure 5. DNP-enhanced ^{1}H→^{13}C spectra at ∼110 K and 21 T of (a) mechanosynthesized n = 1 PEA_2PbI_4 recorded for 2 min (20 min for microwave off) at 50 kHz MAS and (b) a PEAI-treated single thin film of deuterated $FAPbI_3$ recorded for one day at 40 kHz MAS.

PEA^+ signals exhibit enhancement factors of 125 and 35, respectively. Although solvent enhancements up to 200 have been demonstrated with this formulation in pure frozen solutions,[93] the sample enhancement is nevertheless similar to that obtained in the more conventional DNP experiments at 9.4 T above, validating the effectiveness of the experimental setup. We note that a slightly lower sample temperature of 111 K was observed (cf. 119 K at 9.4 T), possibly due to different microwave absorption at higher frequency and/or more efficient cooling of the smaller rotor.

We then turned to the challenge of studying a technologically relevant surface coating on a thin film. Phenylethylammonium iodide (PEAI) is one of the most widely used passivating agents[24,95−97] for perovskite thin films owing to its bulky nature that facilitates the formation of 2D perovskites while providing high stability to the material.[97,98] Here, an ∼500 nm layer of deuterated $FAPbI_3$ was spin-coated onto a glass slide (2 × 2 cm^2) and passivated with a thin (∼20 nm) surface layer of PEAI, followed by annealing at 100 °C.

https://doi.org/10.1021/jacs.2c05316
J. Am. Chem. Soc. 2022, 144, 15175−15184

The film was then scraped off (to yield about 0.8 mg) and packed into a 0.7 mm rotor to which the radical-containing solution was then added by centrifugation. The sample is estimated to contain a total of about 6 μg (50 nmol) of PEA^+. Figure 5b shows that the PEA^+ signals can clearly be seen in the resulting DNP-enhanced $^1H \rightarrow ^{13}C$ spectrum obtained in 27 h, whereas even the most intense peak can barely be seen without DNP, giving an estimated enhancement for the PEA^+ layer by a factor of ~10. (We therefore estimate that it would have taken ~100 days to acquire this spectrum with the same signal-to-noise ratio without DNP.) The FA^+ enhancement is minimal, consistent with expectations from the experiments on deuterated mechanosynthesized $FAPbI_3$. The high PEA^+ enhancement and low FA^+ enhancement are also evident in the ^1H NMR spectrum (Figure S5); however, the resolution is insufficient to interpret the structure, even at 40 kHz MAS.

Comparing the observed PEA^+ carbon-13 shifts (Figures 5 and S3), we note that there is a significant change between the PEAI salt and the n = 1 perovskite, reflecting the substantial structural transformation.[47] The PEA^+ signals observed in the spectra of the surface-coated thin film, as shown in Figure 5b, align most closely with those of the layered perovskites, indicating that after the surface treatment, the PEA^+ adopts the layered perovskite structure, in line with previous reports.[95,97−99] However, the peaks are significantly broader, indicating a broader distribution of local environments and disorder in the thin-film coating. This is consistent with a mixture of n = 1 and higher-order homologues,[54] as well as the nanoscale thickness of the passivating layer, meaning that most of the material is within ~10 nm of the surface or the bulk perovskite, which can slightly modify the local structure. In addition, a slight shift of ~1 ppm is observed for the carbon closest to the perovskite layer (Figure S3). This may correspond to a slightly different binding of the organic spacers to the inorganic layers, or a slight difference in the electronic structure of the inorganic layers, in the nanoscale-coating layer as compared to the bulk layered perovskite.

CONCLUSIONS

In conclusion, we have identified the factors that previously limited DNP efficiency in hybrid perovskites. In particular, we find that the primary impediment to hyperpolarization is the fast ^1H relaxation of the dynamic cation, while microwave absorption by the sample is also detrimental due to both sample heating and reduced saturation efficiency. We have shown that this can be mitigated by deuterating the cation, which then enables large DNP enhancements to develop on both the DNP matrix and target organic species present at low concentrations in the sample. We have further demonstrated that DNP can be favorably applied to two-dimensional layered perovskites, with the high surface-to-volume ratio that can arise from platelet morphologies being particularly beneficial.

There is plenty of further scope to improve the enhancement by optimizing the impregnation protocols, which could be further combined with isotopic labeling to achieve ultimate sensitivity.[73,100,101] This will then enable, for example, multidimensional correlation experiments to provide information about connectivity and spatial proximities.

Here, efficient DNP with deuterated samples enabled the observation of the ^{13}C PEA^+ signals from the approximately 6 μg of surface coating on a single $FAPbI_3$ perovskite thin film, by combining with cutting-edge DNP hardware for small-diameter rotors at a high field. The spectra of the thin film immediately reveal that a 2D PEA^+ layered perovskite structure forms on the bulk perovskite surface that most strongly resembles that in the n = 1 layered perovskite homologue, rather than remaining as PEAI, but with a greater distribution of local environments. This work extends DNP-enhanced solid-state methods to a new class of semiconducting photovoltaic materials and, therefore, paves the way to characterize the local structure of additives and surface treatments for technologically relevant perovskite thin-film compositions.

EXPERIMENTAL SECTION

Materials. The following materials were used: formamidinium iodide (Sigma, >99%), PbI_2 (Sigma, 99%), phenylethylammonium iodide (Greatcell Solar Materials), anhydrous dimethylformamide (99.8%, Acros), dimethylsulfoxide (99.7%, Acros), acetone (99.6%, Acros), chlorobenzene (99.8%, Acros), isopropanol (99.5%, Acros), and d_5-FAI (Cortecnet, 85% CD deuterated, 90% ND_2 deuterated). d_4-FAI and d_3-PEAI were prepared by dissolving in heavy water (1:40 mol/mol ratio), followed by evaporation. This yielded ~50 and ~70% deuterium on the FAI and PEAI, respectively.

Bulk Sample Preparation. The perovskite materials were prepared using mechanosynthesis following a previously published protocol.[48] The precursors (PbI_2, PEAI, and FAI, ~200 mg total) were mixed in the appropriate molar ratio and ground in an electric ball mill (Retsch MM 400) using an agate grinding jar (10 mL) and agate ball (⌀10 mm) for 60 min at 25 Hz. The resulting materials were then annealed at 150 °C for 20 min.

Surface-Coated Thin-Film Fabrication. A 1.4 M solution of d_4-$FAPbI_3$ in 4:1 (v:v) DMF/DMSO ratio was spin-coated onto a glass slide (2 × 2 cm^2) with a two-step program at 1000 and 4000 r.p.m. for 10 and 30 s, respectively. During the second step, 200 μL of chlorobenzene (99.8%, Acros) was dropped onto the spinning substrate 10 s prior to the end of the program and the film was annealed at 150 °C for 20 min. After cooling down the substrate to room temperature, a thin surface layer of d_3-PEAI (5 mg in 1 mL of acetone) was spin-coated on the perovskite layer at 5000 rpm for 30 s, followed by annealing at 100 °C for 5 min.

DNP-Enhanced Solid-State NMR Measurements. DNP formulations, except for the 0.7 mm DNP samples, were prepared according to the standard protocols for impregnation DNP[63−65] by wetting ~50 mg of the perovskite materials with ~50 μL of 16 mM TEKPol[78] in tetrachloroethane (TCE). 1% d_6-EtOH ethanol was included to improve glass formation.[102] For the thin-film formulation, powder was scraped off from the thin film, packed into the 0.7 mm rotor, and then a 32 mM solution of HyTEK-2[94] in TCE was added to the sample by centrifugation at 6000 rpm for a minute.

The majority of the DNP-enhanced spectra were acquired on a commercial Bruker Avance III 400 MHz (9.4 T) NMR spectrometer equipped with a 263 GHz gyrotron microwave source using a 3.2 mm triple resonance low-temperature magic angle spinning (LTMAS) probe with sapphire rotors spinning at 8 kHz. A few grains of KBr were mixed into the material before the impregnation step and the temperature was measured from the ^{79}Br T_1 constant.[103] Before measuring the DNP-enhanced NMR spectra, samples were degassed by performing three insert−eject cycles, waiting for ~1 min at each step. The DNP enhancement factors were measured from the intensity ratio of the $^1H \rightarrow ^{13}C$ cross-polarization (CP)[104] spectra acquired under microwave-on and -off conditions with 100 kHz of SPINAL-64[105] decoupling. A microwave power of ~12 W was used for all DNP experiments, as measured by a calorimeter halfway along the waveguide. ^{13}C chemical shifts were referenced to the TCE peak at 74 ppm at ~100 K.[63,106] The TCE enhancement is reported for a recycle delay of 5 s and the PEA^+/FA^+ enhancements for a recycle delay of 100 s. The ^1H build-up time constants (T_{DNP}) were measured using a saturation-recovery $^1H \rightarrow ^{13}C$ experiment. Errors in the time constants were calculated using Monte-Carlo analysis based on the experimental noise level.

https://doi.org/10.1021/jacs.2c05316
J. Am. Chem. Soc. 2022, 144, 15175−15184

High-field fast-spinning DNP solid-state NMR experiments were performed on a 900 MHz (21.1 T) Avance Neo Bruker NMR spectrometer. The spectrometer was equipped with a LTMAS 0.7 mm triple resonance probe coupled with a Bruker gyrotron producing 593 GHz continuous microwaves. The frequency of the gyrotron was tuned to give the previously observed maximum enhancement for cross-effect DNP with HyTEK-2[94] by modifying the gyrotron cavity temperature to 28°C. The DNP enhancement factors were measured from the intensity ratio of the $^{1}H\rightarrow^{13}C$ cross-polarization (CP) spectra acquired under microwave-on and -off conditions with 110 kHz of SPINAL-64 decoupling. Details specific to particular spectra are given in Table S2 and the figure captions.

X-ray Diffraction (XRD) Measurements. Powder XRD patterns of mechanosynthesized layered and 3D perovskites were recorded with a Bruker D8 Discover Vario diffractometer with a Cu $K\alpha_1$ monochromator (1.5406 Å) from 2θ = 2−50°.

Scanning Electron Microscopy (SEM) Measurements. For the SEM images, mechanosynthesized powders were deposited on a standard SEM sample stub with conductive carbon adhesive tabs. A Zeiss Merlin scanning electron microscope was used, and images were acquired at 0.8 kV beam energy using low currents (20−40 pA) detecting secondary electrons with an in-lens detector. SEM images were analyzed using ImageJ software.

■ ASSOCIATED CONTENT

Supporting Information

The Supporting Information is available free of charge at https://pubs.acs.org/doi/10.1021/jacs.2c05316. All data presented here (raw NMR and XRD data) can be accessed at the following link DOI: 10.5281/zenodo.6962680 and is available under the CC-BY-4.0 (Creative Commons Attribution-ShareAlike 4.0 International) license

Additional $^{1}H\rightarrow^{13}C$, $^{1}H\rightarrow^{15}N$, ^{1}H, and ^{2}H spectra, XRD diffractograms and experimental parameters (PDF)

■ AUTHOR INFORMATION

Corresponding Authors

Michael A. Hope − *Laboratory of Magnetic Resonance, Institut des Sciences et Ingénierie Chimiques, École Polytechnique Fédérale de Lausanne (EPFL), CH-1015 Lausanne, Switzerland;* orcid.org/0000-0002-4742-9336; Email: michael.hope@epfl.ch

Lyndon Emsley − *Laboratory of Magnetic Resonance, Institut des Sciences et Ingénierie Chimiques, École Polytechnique Fédérale de Lausanne (EPFL), CH-1015 Lausanne, Switzerland;* orcid.org/0000-0003-1360-2572; Email: lyndon.emsley@epfl.ch

Authors

Aditya Mishra − *Laboratory of Magnetic Resonance, Institut des Sciences et Ingénierie Chimiques, École Polytechnique Fédérale de Lausanne (EPFL), CH-1015 Lausanne, Switzerland*

Masaud Almalki − *Laboratory of Photonics and Interfaces, Institut des Sciences et Ingénierie Chimiques, École Polytechnique Fédérale de Lausanne (EPFL), CH-1015 Lausanne, Switzerland*

Lukas Pfeifer − *Laboratory of Photonics and Interfaces, Institut des Sciences et Ingénierie Chimiques, École Polytechnique Fédérale de Lausanne (EPFL), CH-1015 Lausanne, Switzerland;* orcid.org/0000-0002-8461-3909

Shaik Mohammed Zakeeruddin − *Laboratory of Photonics and Interfaces, Institut des Sciences et Ingénierie Chimiques, École Polytechnique Fédérale de Lausanne (EPFL), CH-1015 Lausanne, Switzerland*

Michael Grätzel − *Laboratory of Photonics and Interfaces, Institut des Sciences et Ingénierie Chimiques, École Polytechnique Fédérale de Lausanne (EPFL), CH-1015 Lausanne, Switzerland;* orcid.org/0000-0002-0068-0195

Complete contact information is available at: https://pubs.acs.org/10.1021/jacs.2c05316

Notes

The authors declare no competing financial interest.

■ ACKNOWLEDGMENTS

This work was supported by SNSF grant number 200020_178860. M.A.H. acknowledges a H2020 Marie Skłodowska-Curie Individual fellowship with grant number 101024144. M.A. gratefully acknowledges KACST for the fellowship. We thank Dr. Federico De Biasi (EPFL) for stimulating discussions and Dr. Pierrick Berruyer (EPFL) and Dr. Andrea Bertarello (EPFL) for their assistance in performing DNP experiments with 0.7 mm rotors.

■ REFERENCES

(1) Noh, J. H.; Im, S. H.; Heo, J. H.; Mandal, T. N.; Seok, S. I. Chemical Management for Colorful, Efficient, and Stable Inorganic−Organic Hybrid Nanostructured Solar Cells. *Nano Lett.* **2013**, *13*, 1764−1769.

(2) Eperon, G. E.; Stranks, S. D.; Menelaou, C.; Johnston, M. B.; Herz, L.; Snaith, H. Formamidinium Lead Trihalide: A Broadly Tunable Perovskite for Efficient Planar Heterojunction Solar Cells. *Energy Environ. Sci.* **2014**, *7*, 982−988.

(3) Wang, L.; Yuan, G. D.; Duan, R. F.; Huang, F.; Wei, T. B.; Liu, Z. Q.; Wang, J. X.; Li, J. M. Tunable bandgap in hybrid perovskite $CH_3NH_3Pb(Br_{3-y}X_y)$ single crystals and photodetector applications. *AIP Adv.* **2016**, *6*, No. 045115.

(4) Chen, Z.; He, P.; Wu, D.; Chen, C.; Mujahid, M.; Li, Y.; Duan, Y. Processing and Preparation Method for High-Quality Opto-Electronic Perovskite Film. *Front. Mater.* **2021**, *8*, No. 723169.

(5) Ahn, N.; Son, D.-Y.; Jang, I.-H.; Kang, S. M.; Choi, M.; Park, N.-G. Highly Reproducible Perovskite Solar Cells with Average Efficiency of 18.3% and Best Efficiency of 19.7% Fabricated via Lewis Base Adduct of Lead(II) Iodide. *J. Am. Chem. Soc.* **2015**, *137*, 8696−8699.

(6) Jeong, J.; Kim, M.; Seo, J.; Lu, H.; Ahlawat, P.; Mishra, A.; Yang, Y.; Hope, M. A.; Eickemeyer, F. T.; Kim, M.; Yoon, Y. J.; Choi, I. W.; Darwich, B. P.; Choi, S. J.; Jo, Y.; Lee, J. H.; Walker, B.; Zakeeruddin, S. M.; Emsley, L.; Rothlisberger, U.; Hagfeldt, A.; Kim, D. S.; Grätzel, M.; Kim, J. Y. Pseudo-halide anion engineering for α-$FAPbI_3$ perovskite solar cells. *Nature* **2021**, *592*, 381−385.

(7) Lu, H.; Liu, Y.; Ahlawat, P.; Mishra, A.; Tress, W. R.; Eickemeyer, F. T.; Yang, Y.; Fu, F.; Wang, Z.; Avalos, C. E.; Carlsen, B. I.; Agarwalla, A.; Zhang, X.; Li, X.; Zhan, Y.; Zakeeruddin, S. M.; Emsley, L.; Rothlisberger, U.; Zheng, L.; Hagfeldt, A.; Grätzel, M. Vapor-assisted deposition of highly efficient, stable black-phase $FAPbI_3$ perovskite solar cells. *Science* **2020**, *370*, No. eabb8985.

(8) Min, H.; Lee, D. Y.; Kim, J.; Kim, G.; Lee, K. S.; Kim, J.; Paik, M. J.; Kim, Y. K.; Kim, K. S.; Kim, M. G.; Shin, T. J.; Seok, S. I. Perovskite solar cells with atomically coherent interlayers on SnO_2 electrodes. *Nature* **2021**, *598*, 444−450.

(9) Kim, M.; Jeong, J.; Lu, H.; Lee, T. K.; Eickemeyer, F. T.; Liu, Y.; Choi, I. W.; Choi, S. J.; Jo, Y.; Kim, H.-B.; Mo, S.-I.; Kim, Y.-K.; Lee, H.; An, N. G.; Cho, S.; Tress, W. R.; Zakeeruddin, S. M.; Hagfeldt, A.; Kim, J. Y.; Grätzel, M.; Kim, D. S. Conformal quantum dot−SnO_2 layers as electron transporters for efficient perovskite solar cells. *Science* **2022**, *375*, 302−306.

(10) Yoo, J. W.; Jang, J.; Kim, U.; Lee, Y.; Ji, S.-G.; Noh, E.; Hong, S.; Choi, M.; Seok, S. I. Efficient perovskite solar mini-modules

fabricated via bar-coating using 2-methoxyethanol-based formamidinium lead tri-iodide precursor solution. *Joule* **2021**, *5*, 2420−2436.
(11) Yoon, S. M.; Min, H.; Kim, J. B.; Kim, G.; Lee, K. S.; Seok, S. I. Surface Engineering of Ambient-Air-Processed Cesium Lead Triiodide Layers for Efficient Solar Cells. *Joule* **2021**, *5*, 183−196.
(12) Lee, J.-W.; Seol, D.-J.; Cho, A.-N.; Park, N.-G. High-Efficiency Perovskite Solar Cells Based on the Black Polymorph of $HC(NH_2)_2PbI_3$. *Adv. Mater.* **2014**, *26*, 4991−4998.
(13) Park, Y. H.; Jeong, I.; Bae, S.; Son, H. J.; Lee, P.; Lee, J.; Lee, C. H.; Ko, M. J. Inorganic Rubidium Cation as an Enhancer for Photovoltaic Performance and Moisture Stability of $HC(NH_2)_2PbI_3$ Perovskite Solar Cells. *Adv. Funct. Mater.* **2017**, *27*, No. 1605988.
(14) Pellet, N.; Gao, P.; Gregori, G.; Yang, T. Y.; Nazeeruddin, M. K.; Maier, J.; Grätzel, M. Mixed-organic-cation perovskite photovoltaics for enhanced solar-light harvesting. *Angew. Chem., Int. Ed.* **2014**, *53*, 3151−3157.
(15) Lee, J.-W.; Kim, D.-H.; Kim, H.-S.; Seo, S.-W.; Cho, S. M.; Park, N.-G. Formamidinium and Cesium Hybridization for Photo- and Moisture-Stable Perovskite Solar Cell. *Adv. Energy Mater.* **2015**, *5*, No. 1501310.
(16) De Marco, N.; Zhou, H.; Chen, Q.; Sun, P.; Liu, Z.; Meng, L.; Yao, E. P.; Liu, Y.; Schiffer, A.; Yang, Y. Guanidinium: A Route to Enhanced Carrier Lifetime and Open-Circuit Voltage in Hybrid Perovskite Solar Cells. *Nano Lett.* **2016**, *16*, 1009−1016.
(17) Jodlowski, A. D.; Roldán-Carmona, C.; Grancini, G.; Salado, M.; Ralaiarisoa, M.; Ahmad, S.; Koch, N.; Camacho, L.; De Miguel, G.; Nazeeruddin, M. K. Large Guanidinium Cation Mixed with Methylammonium in Lead Iodide Perovskites for 19% Efficient Solar Cells. *Nat. Energy* **2017**, *2*, 972−979.
(18) Hsu, H.-L.; Chang, C.-C.; Chen, C.-P.; Jiang, B.-H.; Jeng, R.-J.; Cheng, C.-H. High-performance and high-durability perovskite photovoltaic devices prepared using ethylammonium iodide as an additive. *J. Mater. Chem. A* **2015**, *3*, 9271−9277.
(19) Wang, Q.; Lin, F.; Chueh, C.-C.; Zhao, T.; Eslamian, M.; Jen, A. K. Y. Enhancing efficiency of perovskite solar cells by reducing defects through imidazolium cation incorporation. *Mater. Today Energy* **2018**, *7*, 161−168.
(20) Milić, J. V.; Zakeeruddin, S. M.; Grätzel, M. Layered Hybrid Formamidinium Lead Iodide Perovskites: Challenges and Opportunities. *Acc. Chem. Res.* **2021**, *54*, 2729−2740.
(21) Saparov, B.; Mitzi, D. B. Organic−Inorganic Perovskites: Structural Versatility for Functional Materials Design. *Chem. Rev.* **2016**, *116*, 4558−4596.
(22) Mao, L.; Stoumpos, C. C.; Kanatzidis, M. G. Two-Dimensional Hybrid Halide Perovskites: Principles and Promises. *J. Am. Chem. Soc.* **2019**, *141*, 1171−1190.
(23) Grancini, G.; Nazeeruddin, M. K. Dimensional tailoring of hybrid perovskites for photovoltaics. *Nat. Rev. Mater.* **2019**, *4*, 4−22.
(24) Smith, I. C.; Hoke, E. T.; Solis-Ibarra, D.; McGehee, M. D.; Karunadasa, H. I. A Layered Hybrid Perovskite Solar-Cell Absorber with Enhanced Moisture Stability. *Angew. Chem., Int. Ed.* **2014**, *53*, 11232−11235.
(25) Huang, Y.; Li, Y.; Lim, E. L.; Kong, T.; Zhang, Y.; Song, J.; Hagfeldt, A.; Bi, D. Stable Layered 2D Perovskite Solar Cells with an Efficiency of over 19% via Multifunctional Interfacial Engineering. *J. Am. Chem. Soc.* **2021**, *143*, 3911−3917.
(26) Li, Y.; Wu, H.; Qi, W.; Zhou, X.; Li, J.; Cheng, J.; Zhao, Y.; Li, Y.; Zhang, X. Passivation of defects in perovskite solar cell: From a chemistry point of view. *Nano Energy* **2020**, *77*, No. 105237.
(27) Liu, Y.; Akin, S.; Pan, L.; Uchida, R.; Arora, N.; Milić, J. V.; Hinderhofer, A.; Schreiber, F.; Uhl, A. R.; Zakeeruddin, S. M.; Hagfeldt, A.; Dar, M. I.; Grätzel, M. Ultrahydrophobic 3D/2D fluoroarene bilayer-based water-resistant perovskite solar cells with efficiencies exceeding 22%. *Sci. Adv.* **2019**, *5*, No. eaaw2543.
(28) Chen, H.; Teale, S.; Chen, B.; Hou, Y.; Grater, L.; Zhu, T.; Bertens, K.; Park, S. M.; Atapattu, H. R.; Gao, Y.; Wei, M.; Johnston, A. K.; Zhou, Q.; Xu, K.; Yu, D.; Han, C.; Cui, T.; Jung, E. H.; Zhou, C.; Zhou, W.; Proppe, A. H.; Hoogland, S.; Laquai, F.; Filleter, T.; Graham, K. R.; Ning, Z.; Sargent, E. H. Quantum-size-tuned heterostructures enable efficient and stable inverted perovskite solar cells. *Nat. Photonics* **2022**, *16*, 352−358.
(29) Zhang, F.; Park, S. Y.; Yao, C.; Lu, H.; Dunfield, S. P.; Xiao, C.; Uličná, S.; Zhao, X.; Hill, L. D.; Chen, X.; Wang, X.; Mundt, L. E.; Stone, K. H.; Schelhas, L. T.; Teeter, G.; Parkin, S.; Ratcliff, E. L.; Loo, Y.-L.; Berry, J. J.; Beard, M. C.; Yan, Y.; Larson, B. W.; Zhu, K. Metastable Dion-Jacobson 2D structure enables efficient and stable perovskite solar cells. *Science* **2022**, *375*, 71−76.
(30) Bi, D.; Li, X.; Milić, J. V.; Kubicki, D. J.; Pellet, N.; Luo, J.; LaGrange, T.; Mettraux, P.; Emsley, L.; Zakeeruddin, S. M.; Grätzel, M. Multifunctional Molecular Modulators for Perovskite Solar Cells with over 20% Efficiency and High Operational Stability. *Nat. Commun.* **2018**, *9*, No. 4482.
(31) Alanazi, A. Q.; Kubicki, D. J.; Prochowicz, D.; Alharbi, E. A.; Bouduban, M. E. F.; Jahanbakhshi, F.; Mladenović, M.; Milić, J. V.; Giordano, F.; Ren, D.; Alyamani, A. Y.; Albrithen, H.; Albadri, A.; Alotaibi, M. H.; Moser, J. E.; Zakeeruddin, S. M.; Rothlisberger, U.; Emsley, L.; Grätzel, M. Atomic-Level Microstructure of Efficient Formamidinium-Based Perovskite Solar Cells Stabilized by 5-Ammonium Valeric Acid Iodide Revealed by Multinuclear and Two-Dimensional Solid-State NMR. *J. Am. Chem. Soc.* **2019**, *141*, 17659−17669.
(32) Kubicki, D. J.; Stranks, S. D.; Grey, C. P.; Emsley, L. NMR spectroscopy probes microstructure, dynamics and doping of metal halide perovskites. *Nat. Rev. Chem.* **2021**, *5*, 624−645.
(33) Dahlman, C. J.; Kubicki, D. J.; Reddy, G. N. M. Interfaces in metal halide perovskites probed by solid-state NMR spectroscopy. *J. Mater. Chem. A* **2021**, *9*, 19206−19244.
(34) Reif, B.; Ashbrook, S. E.; Emsley, L.; Hong, M. Solid-state NMR spectroscopy. *Nat. Rev. Methods Primers* **2021**, *1*, No. 2.
(35) Franssen, W. M. J.; Kentgens, A. P. M. Solid−state NMR of hybrid halide perovskites. *Solid State Nucl. Magn. Reson.* **2019**, *100*, 36−44.
(36) Kubicki, D. J.; Prochowicz, D.; Hofstetter, A.; Zakeeruddin, S. M.; Grätzel, M.; Emsley, L. Phase Segregation in Cs-, Rb- and K-Doped Mixed-Cation $(MA)_x(FA)_{1-x}PbI_3$ Hybrid Perovskites from Solid-State NMR. *J. Am. Chem. Soc.* **2017**, *139*, 14173−14180.
(37) Kubicki, D. J.; Prochowicz, D.; Hofstetter, A.; Saski, M.; Yadav, P.; Bi, D.; Pellet, N.; Lewiński, J.; Zakeeruddin, S. M.; Grätzel, M.; Emsley, L. Formation of Stable Mixed Guanidinium−Methylammonium Phases with Exceptionally Long Carrier Lifetimes for High-Efficiency Lead Iodide-Based Perovskite Photovoltaics. *J. Am. Chem. Soc.* **2018**, *140*, 3345−3351.
(38) Kubicki, D. J.; Prochowicz, D.; Hofstetter, A.; Zakeeruddin, S. M.; Grätzel, M.; Emsley, L. Phase Segregation in Potassium-Doped Lead Halide Perovskites from ^{39}K Solid-State NMR at 21.1 T. *J. Am. Chem. Soc.* **2018**, *140*, 7232−7238.
(39) Franssen, W. M. J.; Bruijnaers, B. J.; Portengen, V. H. L.; Kentgens, A. P. M. Dimethylammonium Incorporation in Lead Acetate Based $MAPbI_3$ Perovskite Solar Cells. *ChemPhysChem* **2018**, *19*, 3107−3115.
(40) Nayak, P. K.; Sendner, M.; Wenger, B.; Wang, Z.; Sharma, K.; Ramadan, A. J.; Lovrinčić, R.; Pucci, A.; Madhu, P. K.; Snaith, H. J. Impact of Bi^{3+} Heterovalent Doping in Organic−Inorganic Metal Halide Perovskite Crystals. *J. Am. Chem. Soc.* **2018**, *140*, 574−577.
(41) Boziki, A.; Kubicki, D. J.; Mishra, A.; Meloni, S.; Emsley, L.; Grätzel, M.; Rothlisberger, U. Atomistic Origins of the Limited Phase Stability of Cs^+-Rich $FA_xCs_{(1-x)}PbI_3$ Mixtures. *Chem. Mater.* **2020**, *32*, 2605−2614.
(42) Kubicki, D. J.; Prochowicz, D.; Pinon, A.; Stevanato, G.; Hofstetter, A.; Zakeeruddin, S. M.; Grätzel, M.; Emsley, L. Doping and Phase Segregation in Mn^{2+} - and Co^{2+} -Doped Lead Halide Perovskites from ^{133}Cs and ^{1}H NMR Relaxation Enhancement. *J. Mater. Chem. A* **2019**, *7*, 2326−2333.
(43) Karmakar, A.; Dodd, M. S.; Zhang, X.; Oakley, M. S.; Klobukowski, M.; Michaelis, V. K. Mechanochemical synthesis of 0D and 3D cesium lead mixed halide perovskites. *Chem. Commun.* **2019**, *55*, 5079−5082.

https://doi.org/10.1021/jacs.2c05316
J. Am. Chem. Soc. 2022, 144, 15175−15184

(44) Karmakar, A.; Bhattacharya, A.; Bernard, G. M.; Mar, A.; Michaelis, V. K. Revealing the Local Sn and Pb Arrangements in $CsSn_xPb_{1-x}Br_3$ Perovskites with Solid-State NMR Spectroscopy. *ACS Mater. Lett.* **2021**, *3*, 261−267.
(45) Rosales, B. A.; Hanrahan, M. P.; Boote, B. W.; Rossini, A. J.; Smith, E. A.; Vela, J. Lead Halide Perovskites: Challenges and Opportunities in Advanced Synthesis and Spectroscopy. *ACS Energy Lett.* **2017**, *2*, 906−914.
(46) Rosales, B. A.; Men, L.; Cady, S. D.; Hanrahan, M. P.; Rossini, A. J.; Vela, J. Persistent Dopants and Phase Segregation in Organolead Mixed-Halide Perovskites. *Chem. Mater.* **2016**, *28*, 6848−6859.
(47) Hope, M. A.; Nakamura, T.; Ahlawat, P.; Mishra, A.; Cordova, M.; Jahanbakhshi, F.; Mladenović, M.; Runjhun, R.; Merten, L.; Hinderhofer, A.; Carlsen, B. I.; Kubicki, D. J.; Gershoni-Poranne, R.; Schneeberger, T.; Carbone, L. C.; Liu, Y.; Zakeeruddin, S. M.; Lewinski, J.; Hagfeldt, A.; Schreiber, F.; Rothlisberger, U.; Grätzel, M.; Milić, J. V.; Emsley, L. Nanoscale Phase Segregation in Supramolecular π-Templating for Hybrid Perovskite Photovoltaics from NMR Crystallography. *J. Am. Chem. Soc.* **2021**, *143*, 1529−1538.
(48) Kubicki, D. J.; Prochowicz, D.; Hofstetter, A.; Péchy, P.; Zakeeruddin, S. M.; Grätzel, M.; Emsley, L. Cation Dynamics in Mixed-Cation $(MA)_x(FA)_{1-x}PbI_3$ Hybrid Perovskites from Solid-State NMR. *J. Am. Chem. Soc.* **2017**, *139*, 10055−10061.
(49) Fabini, D. H.; Siaw, T. A.; Stoumpos, C. C.; Laurita, G.; Olds, D.; Page, K.; Hu, J. G.; Kanatzidis, M. G.; Han, S.; Seshadri, R. Universal Dynamics of Molecular Reorientation in Hybrid Lead Iodide Perovskites. *J. Am. Chem. Soc.* **2017**, *139*, 16875−16884.
(50) Bernard, G. M.; Wasylishen, R. E.; Ratcliffe, C. I.; Terskikh, V.; Wu, Q.; Buriak, J. M.; Hauger, T. Methylammonium Cation Dynamics in Methylammonium Lead Halide Perovskites: A Solid-State NMR Perspective. *J. Phys. Chem. A* **2018**, *122*, 1560−1573.
(51) Mozur, E. M.; Hope, M. A.; Trowbridge, J. C.; Halat, D. M.; Daemen, L. L.; Maughan, A. E.; Prisk, T. R.; Grey, C. P.; Neilson, J. R. Cesium Substitution Disrupts Concerted Cation Dynamics in Formamidinium Hybrid Perovskites. *Chem. Mater.* **2020**, *32*, 6266−6277.
(52) Kazemi, M. A. A.; Raval, P.; Cherednichekno, K.; Chotard, J.-N.; Krishna, A.; Demortiere, A.; Reddy, G. N. M.; Sauvage, F. Molecular-Level Insight into Correlation between Surface Defects and Stability of Methylammonium Lead Halide Perovskite Under Controlled Humidity. *Small Methods* **2021**, *5*, No. 2000834.
(53) Raval, P.; Kennard, R. M.; Vasileiadou, E. S.; Dahlman, C. J.; Spanopoulos, I.; Chabinyc, M. L.; Kanatzidis, M.; Reddy, G. N. M. Understanding Instability in Formamidinium Lead Halide Perovskites: Kinetics of Transformative Reactions at Grain and Subgrain Boundaries. *ACS Energy Lett.* **2022**, *7*, 1534−1543.
(54) Milić, J. V.; Im, J.; Kubicki, D. J.; Ummadisingu, A.; Seo, J.; Li, Y.; Ruiz Preciado, M. A.; Dar, M. I.; Zakeeruddin, S. M.; Emsley, L.; Grätzel, M. Supramolecular Engineering for Formamidinium Based Layered 2D Perovskite Solar Cells: Structural Complexity and Dynamics Revealed by Solid State NMR Spectroscopy. *Adv. Energy Mater.* **2019**, *9*, No. 1900284.
(55) Mishra, A.; Ahlawat, P.; Fish, G. C.; Jahanbakhshi, F.; Mladenović, M.; Almalki, M.; Ruiz-Preciado, M. A.; Gelvéz-Rueda, M. C.; Kubicki, D. J.; Schouwink, P. A.; Dufoulon, V.; Schneeberger, T.; Aslanzadeh, A.; Grozema, F. C.; Zakeeruddin, S. M.; Moser, J.-E.; Rothlisberger, U.; Emsley, L.; Milić, J. V.; Grätzel, M. Naphthalenediimide/Formamidinium-Based Low-Dimensional Perovskites. *Chem. Mater.* **2021**, *33*, 6412−6420.
(56) Alanazi, A. Q.; Almalki, M. H.; Mishra, A.; Kubicki, D. J.; Wang, Z.; Merten, L.; Eickemeyer, F. T.; Zhang, H.; Ren, D.; Alyamani, A. Y.; Albrithen, H.; Albadri, A.; Alotaibi, M. H.; Hinderhofer, A.; Zakeeruddin, S. M.; Schreiber, F.; Hagfeldt, A.; Emsley, L.; Milić, J. V.; Grätzel, M. Benzylammonium-Mediated Formamidinium Lead Iodide Perovskite Phase Stabilization for Photovoltaics. *Adv. Funct. Mater.* **2021**, *31*, No. 2101163.
(57) Ummadisingu, A.; Mishra, A.; Kubicki, D. J.; LaGrange, T.; Dučinskas, A.; Siczek, M.; Bury, W.; Milić, J. V.; Grätzel, M.; Emsley, L. Multi-Length Scale Structure of 2D/3D Dion−Jacobson Hybrid Perovskites Based on an Aromatic Diammonium Spacer. *Small* **2022**, *18*, No. 2104287.
(58) Ruiz-Preciado, M. A.; Kubicki, D. J.; Hofstetter, A.; McGovern, L.; Futscher, M. H.; Ummadisingu, A.; Gershoni-Poranne, R.; Zakeeruddin, S. M.; Ehrler, B.; Emsley, L.; Milić, J. V.; Grätzel, M. Supramolecular Modulation of Hybrid Perovskite Solar Cells via Bifunctional Halogen Bonding Revealed by Two-Dimensional ^{19}F Solid-State NMR Spectroscopy. *J. Am. Chem. Soc.* **2020**, *142*, 1645−1654.
(59) Wang, Z.; Lin, Q.; Chmiel, F. P.; Sakai, N.; Herz, L. M.; Snaith, H. J. Efficient ambient-air-stable solar cells with 2D−3D heterostructured butylammonium-caesium-formamidinium lead halide perovskites. *Nat. Energy* **2017**, *2*, No. 17135.
(60) Chen, Y.; Smock, S. R.; Flintgruber, A. H.; Perras, F. A.; Brutchey, R. L.; Rossini, A. J. Surface Termination of $CsPbBr_3$ Perovskite Quantum Dots Determined by Solid-State NMR Spectroscopy. *J. Am. Chem. Soc.* **2020**, *142*, 6117−6127.
(61) Brown, A. A. M.; Hooper, T. J. N.; Veldhuis, S. A.; Chin, X. Y.; Bruno, A.; Vashishtha, P.; Tey, J. N.; Jiang, L.; Damodaran, B.; Pu, S. H.; Mhaisalkar, S. G.; Mathews, N. Self-assembly of a robust hydrogen-bonded octylphosphonate network on cesium lead bromide perovskite nanocrystals for light-emitting diodes. *Nanoscale* **2019**, *11*, 12370−12380.
(62) Hooper, T. J. N.; Fang, Y.; Brown, A. A. M.; Pu, S. H.; White, T. J. Structure and surface properties of size-tuneable $CsPbBr_3$ nanocrystals. *Nanoscale* **2021**, *13*, 15770−15780.
(63) Rossini, A. J.; Zagdoun, A.; Hegner, F.; Schwarzwälder, M.; Gajan, D.; Copéret, C.; Lesage, A.; Emsley, L. Dynamic Nuclear Polarization NMR Spectroscopy of Microcrystalline Solids. *J. Am. Chem. Soc.* **2012**, *134*, 16899−16908.
(64) Rossini, A. J.; Zagdoun, A.; Lelli, M.; Lesage, A.; Copéret, C.; Emsley, L. Dynamic Nuclear Polarization Surface Enhanced NMR Spectroscopy. *Acc. Chem. Res.* **2013**, *46*, 1942−1951.
(65) Lesage, A.; Lelli, M.; Gajan, D.; Caporini, M. A.; Vitzthum, V.; Miéville, P.; Alauzun, J.; Roussey, A.; Thieuleux, C.; Mehdi, A.; Bodenhausen, G.; Coperet, C.; Emsley, L. Surface Enhanced NMR Spectroscopy by Dynamic Nuclear Polarization. *J. Am. Chem. Soc.* **2010**, *132*, 15459−15461.
(66) Ni, Q. Z.; Daviso, E.; Can, T. V.; Markhasin, E.; Jawla, S. K.; Swager, T. M.; Temkin, R. J.; Herzfeld, J.; Griffin, R. G. High Frequency Dynamic Nuclear Polarization. *Acc. Chem. Res.* **2013**, *46*, 1933−1941.
(67) Thankamony, A. S. L.; Wittmann, J. J.; Kaushik, M.; Corzilius, B. Dynamic nuclear polarization for sensitivity enhancement in modern solid-state NMR. *Prog. Nucl. Magn. Reson. Spectrosc.* **2017**, *102*−*103*, 120−195.
(68) Haber, S.; Leskes, M. Dynamic Nuclear Polarization in battery materials. *Solid State Nucl. Magn. Reson.* **2022**, *117*, No. 101763.
(69) Leskes, M.; Kim, G.; Liu, T.; Michan, A. L.; Aussenac, F.; Dorffer, P.; Paul, S.; Grey, C. P. Surface-Sensitive NMR Detection of the Solid Electrolyte Interphase Layer on Reduced Graphene Oxide. *J. Phys. Chem. Lett.* **2017**, *8*, 1078−1085.
(70) Kobayashi, T.; Perras, F. A.; Slowing, I. I.; Sadow, A. D.; Pruski, M. Dynamic Nuclear Polarization Solid-State NMR in Heterogeneous Catalysis Research. *ACS Catal.* **2015**, *5*, 7055−7062.
(71) Blanc, F. Investigation of Catalytic Surfaces with Surface-Enhanced Solid-State NMR Spectroscopy. In *Nanotechnology in Catalysis*, Van de Voorde, M.; Sels, B., Eds.; Wiley-VCH: Weinheim, 2017; pp 1003−1028.
(72) Liao, W.-C.; Ghaffari, B.; Gordon, C. P.; Xu, J.; Copéret, C. Dynamic Nuclear Polarization Surface Enhanced NMR spectroscopy (DNP SENS): Principles, protocols, and practice. *Curr. Opin. Colloid Interface Sci.* **2018**, *33*, 63−71.
(73) Berruyer, P.; Lelli, M.; Conley, M. P.; Silverio, D. L.; Widdifield, C. M.; Siddiqi, G.; Gajan, D.; Lesage, A.; Copéret, C.; Emsley, L. Three-Dimensional Structure Determination of Surface Sites. *J. Am. Chem. Soc.* **2017**, *139*, 849−855.
(74) Venkatesh, A.; Lund, A.; Rochlitz, L.; Jabbour, R.; Gordon, C. P.; Menzildjian, G.; Viger-Gravel, J.; Berruyer, P.; Gajan, D.; Copéret,

C.; Lesage, A.; Rossini, A. J. The Structure of Molecular and Surface Platinum Sites Determined by DNP-SENS and Fast MAS ^{195}Pt Solid-State NMR Spectroscopy. *J. Am. Chem. Soc.* **2020**, *142*, 18936−18945.
(75) Lee, D.; Duong, N. T.; Lafon, O.; De Paëpe, G. Primostrato Solid-State NMR Enhanced by Dynamic Nuclear Polarization: Pentacoordinated Al^{3+} Ions Are Only Located at the Surface of Hydrated γ-Alumina. *J. Phys. Chem. C* **2014**, *118*, 25065−25076.
(76) Piveteau, L.; Ong, T.-C.; Rossini, A. J.; Emsley, L.; Copéret, C.; Kovalenko, M. V. Structure of Colloidal Quantum Dots from Dynamic Nuclear Polarization Surface Enhanced NMR Spectroscopy. *J. Am. Chem. Soc.* **2015**, *137*, 13964−13971.
(77) Hanrahan, M. P.; Men, L.; Rosales, B. A.; Vela, J.; Rossini, A. J. Sensitivity-Enhanced ^{207}Pb Solid-State NMR Spectroscopy for the Rapid, Non-Destructive Characterization of Organolead Halide Perovskites. *Chem. Mater.* **2018**, *30*, 7005−7015.
(78) Zagdoun, A.; Casano, G.; Ouari, O.; Schwarzwälder, M.; Rossini, A. J.; Aussenac, F.; Yulikov, M.; Jeschke, G.; Copéret, C.; Lesage, A.; Tordo, P.; Emsley, L. Large Molecular Weight Nitroxide Biradicals Providing Efficient Dynamic Nuclear Polarization at Temperatures up to 200 K. *J. Am. Chem. Soc.* **2013**, *135*, 12790−12797.
(79) Zagdoun, A.; Rossini, A. J.; Gajan, D.; Bourdolle, A.; Ouari, O.; Rosay, M.; Maas, W. E.; Tordo, P.; Lelli, M.; Emsley, L.; Lesage, A.; Copéret, C. Non-aqueous solvents for DNP surface enhanced NMR spectroscopy. *Chem. Commun.* **2012**, *48*, 654−656.
(80) Kawachi, S.; Atsumi, M.; Saito, N.; Ohashi, N.; Murakami, Y.; Yamaura, J.-i. Structural and Thermal Properties in Formamidinium and Cs-Mixed Lead Halides. *J. Phys. Chem. Lett.* **2019**, *10*, 6967−6972.
(81) Walder, B. J.; Berk, C.; Liao, W.-C.; Rossini, A. J.; Schwarzwälder, M.; Pradere, U.; Hall, J.; Lesage, A.; Copéret, C.; Emsley, L. One- and Two-Dimensional High-Resolution NMR from Flat Surfaces. *ACS Cent. Sci.* **2019**, *5*, 515−523.
(82) Zhao, L.; Pinon, A. C.; Emsley, L.; Rossini, A. J. DNP-enhanced solid-state NMR spectroscopy of active pharmaceutical ingredients. *Magn. Reson. Chem.* **2018**, *56*, 583−609.
(83) Lecina, O. S.; Hope, M. A.; Venkatesh, A.; Björgvinsdóttir, S.; Rossi, K.; Loiudice, A.; Emsley, L.; Buonsanti, R. Colloidal-ALD-Grown Hybrid Shells Nucleate via a Ligand−Precursor Complex. *J. Am. Chem. Soc.* **2022**, *144*, 3998−4008.
(84) Poglitsch, A.; Weber, D. Dynamic disorder in methylammoniumtrihalogenoplumbates (II) observed by millimeter-wave spectroscopy. *J. Chem. Phys.* **1987**, *87*, 6373−6378.
(85) Ripolles, T. S.; Serafini, P.; Redondo-Obispo, C.; Climent-Pascual, E.; Masi, S.; Mora-Seró, I.; Coya, C. Interface Engineering in Perovskite Solar Cells by Low Concentration of Phenylethyl Ammonium Iodide Solution in the Antisolvent Step. *Energy Technol.* **2022**, *10*, No. 2100890.
(86) Lee, D. S.; Yun, J. S.; Kim, J.; Soufiani, A. M.; Chen, S.; Cho, Y.; Deng, X.; Seidel, J.; Lim, S.; Huang, S.; Ho-Baillie, A. W. Y. Passivation of grain boundaries by phenethylammonium in formamidinium-methylammonium lead halide perovskite solar cells. *ACS Energy Lett.* **2018**, *3*, 647−654.
(87) Pinon, A. C.; Schlagnitweit, J.; Berruyer, P.; Rossini, A. J.; Lelli, M.; Socie, E.; Tang, M.; Pham, T.; Lesage, A.; Schantz, S.; Emsley, L. Measuring Nano- to Microstructures from Relayed Dynamic Nuclear Polarization NMR. *J. Phys. Chem. C* **2017**, *121*, 15993−16005.
(88) Prisco, N. A.; Pinon, A. C.; Emsley, L.; Chmelka, B. F. Scaling analyses for hyperpolarization transfer across a spin-diffusion barrier and into bulk solid media. *Phys. Chem. Chem. Phys* **2021**, *23*, 1006−1020.
(89) Rosay, M. M. *Sensitivity-Enhanced Nuclear Magnetic Resonance of Biological Solids*; Dissertation, Massachusetts Institute of Technology (MIT): Cambridge, USA, 2001.
(90) Hu, K.-N.; Yu, H.-h.; Swager, T. M.; Griffin, R. G. Dynamic Nuclear Polarization with Biradicals. *J. Am. Chem. Soc.* **2004**, *126*, 10844−10845.
(91) Akbey, Ü.; Franks, W. T.; Linden, A.; Lange, S.; Griffin, R. G.; van Rossum, B.-J.; Oschkinat, H. Dynamic Nuclear Polarization of Deuterated Proteins. *Angew. Chem., Int. Ed.* **2010**, *49*, 7803−7806.
(92) Zagdoun, A.; Rossini, A. J.; Conley, M. P.; Grüning, W. R.; Schwarzwälder, M.; Lelli, M.; Franks, W. T.; Oschkinat, H.; Copéret, C.; Emsley, L.; Lesage, A. Improved Dynamic Nuclear Polarization Surface-Enhanced NMR Spectroscopy through Controlled Incorporation of Deuterated Functional Groups. *Angew. Chem., Int. Ed.* **2013**, *52*, 1222−1225.
(93) Berruyer, P.; Björgvinsdóttir, S.; Bertarello, A.; Stevanato, G.; Rao, Y.; Karthikeyan, G.; Casano, G.; Ouari, O.; Lelli, M.; Reiter, C.; Engelke, F.; Emsley, L. Dynamic Nuclear Polarization Enhancement of 200 at 21.15 T Enabled by 65 kHz Magic Angle Spinning. *J. Phys. Chem. Lett.* **2020**, *11*, 8386−8391.
(94) Wisser, D.; Karthikeyan, G.; Lund, A.; Casano, G.; Karoui, H.; Yulikov, M.; Menzildjian, G.; Pinon, A. C.; Purea, A.; Engelke, F.; Chaudhari, S. R.; Kubicki, D.; Rossini, A. J.; Moroz, I. B.; Gajan, D.; Copéret, C.; Jeschke, G.; Lelli, M.; Emsley, L.; Lesage, A.; Ouari, O. BDPA-Nitroxide Biradicals Tailored for Efficient Dynamic Nuclear Polarization Enhanced Solid-State NMR at Magnetic Fields up to 21.1 T. *J. Am. Chem. Soc.* **2018**, *140*, 13340−13349.
(95) Li, N.; Zhu, Z.; Chueh, C. C.; Liu, H.; Peng, B.; Petrone, A.; Li, X.; Wang, L.; Jen, A. K. Y. Mixed Cation $FA_xPEA_{1-x}PbI3$ with Enhanced Phase and Ambient Stability toward High-Performance Perovskite Solar Cells. *Adv. Energy Mater.* **2017**, *7*, No. 1601307.
(96) Quan, L. N.; Yuan, M.; Comin, R.; Voznyy, O.; Beauregard, E. M.; Hoogland, S.; Buin, A.; Kirmani, A. R.; Zhao, K.; Amassian, A.; et al. Ligand-Stabilized Reduced-Dimensionality Perovskites. *J. Am. Chem. Soc.* **2016**, *138*, 2649−2655.
(97) Jiang, Q.; Zhao, Y.; Zhang, X.; Yang, X.; Chen, Y.; Chu, Z.; Ye, Q.; Li, X.; Yin, Z.; You, J. Surface passivation of perovskite film for efficient solar cells. *Nat. Photonics* **2019**, *13*, 460−466.
(98) Cho, K. T.; Grancini, G.; Lee, Y.; Oveisi, E.; Ryu, J.; Almora, O.; Tschumi, M.; Schouwink, P. A.; Seo, G.; Heo, S.; Park, J.; Jang, J.; Paek, S.; Garcia-Belmonte, G.; Nazeeruddin, M. K. Selective growth of layered perovskites for stable and efficient photovoltaics. *Energy Environ. Sci.* **2018**, *11*, 952−959.
(99) Lee, J.-W.; Dai, Z.; Han, T.-H.; Choi, C.; Chang, S.-Y.; Lee, S.-J.; De Marco, N.; Zhao, H.; Sun, P.; Huang, Y.; Yang, Y. 2D perovskite stabilized phase-pure formamidinium perovskite solar cells. *Nat. Commun.* **2018**, *9*, No. 3021.
(100) Sangodkar, R. P.; Smith, B. J.; Gajan, D.; Rossini, A. J.; Roberts, L. R.; Funkhouser, G. P.; Lesage, A.; Emsley, L.; Chmelka, B. F. Influences of Dilute Organic Adsorbates on the Hydration of Low-Surface-Area Silicates. *J. Am. Chem. Soc.* **2015**, *137*, 8096−8112.
(101) Perras, F. A.; Boteju, K. C.; Slowing, I. I.; Sadow, A. D.; Pruski, M. Direct ^{17}O dynamic nuclear polarization of single-site heterogeneous catalysts. *Chem. Commun.* **2018**, *54*, 3472−3475.
(102) Eaton, G. R.; Eaton, S. S.; Barr, D. P.; Weber, R. T. *Quantitative EPR*; Springer Science & Business Media, 2010.
(103) Thurber, K. R.; Tycko, R. Measurement of sample temperatures under magic-angle spinning from the chemical shift and spin-lattice relaxation rate of ^{79}Br in KBr powder. *J. Magn. Reson.* **2009**, *196*, 84−87.
(104) Pines, A.; Gibby, M. G.; Waugh, J. S. Proton-enhanced NMR of dilute spins in solids. *J. Chem. Phys.* **1973**, *59*, 569−590.
(105) Fung, B. M.; Khitrin, A. K.; Ermolaev, K. An Improved Broadband Decoupling Sequence for Liquid Crystals and Solids. *J. Magn. Reson.* **2000**, *142*, 97−101.
(106) Yarava, J. R.; Chaudhari, S. R.; Rossini, A. J.; Lesage, A.; Emsley, L. Solvent suppression in DNP enhanced solid state NMR. *J. Magn. Reson.* **2017**, *277*, 149−153.

https://doi.org/10.1021/jacs.2c05316
J. Am. Chem. Soc. 2022, 144, 15175−15184